Article

Insight into the Internal Structure of High-Performance Multicore Magnetic Nanoparticles Used in Cancer Thermotherapy

Tom Roussel, Daniel Ferry, Artemis Kosta, Dalila Miele, Giuseppina Sandri, Felista L. Tansi, Frank Steiniger, Paul Southern, Quentin A. Pankhurst,* Ling Peng,* and Suzanne Giorgio*

Cite This: ACS Mater. Au 2024, 4, 489−499

Read Online

| ACCESS | Metrics & More | Article Recommendations | Supporting Information |

ABSTRACT: Multicore magnetic nanoparticles (MNPs), comprising iron oxide cores embedded in a sugar or starch matrix, are a class of nanomaterials with promising magnetic heating properties. Their internal structure, and particularly the strength of the internal core−core magnetic interactions, are believed to determine the functional properties, but there have been few detailed studies on this to date. We report here on an interlaboratory and multimodality transmission electron microscopy (TEM) and magnetic study of a high-performance MNP material (supplied by Resonant Circuits Limited, RCL) that is currently being used in a clinical study for the treatment of pancreatic cancer. TEM data were collected under a variety of conditions: conventional; high-resolution; scanning; cryogenic; and, for the first time, liquid phase. All the imaging modes showed mostly irregular dextran lamellae of lateral dimensions 30−90 nm, plus ca. 15% n/n of what appeared to be 30−60 nm long "nanorods", and a multitude of well-dispersed ca. 3.7 nm diameter iron oxide cores. Cryogenic electron tomography indicated that the nanorods were edge-on lamellae, but in dried samples, tomography showed rod- or lath-shaped forms, possibly resulting from the collapse of lamellae during drying. High-resolution TEM (HRTEM) showed the dextran to be crystallized in the low-temperature hydrated dextran polymorph. Magnetic remanence Henkel-plot analysis indicated a weak core−core interaction field of ca. 4.8 kA/m. Theoretical estimates using a point-dipole model associated this field with a core-to-core separation distance of ca. 5 nm, which tallies well with the ca. 4−6 nm range of separation distances observed in liquid-cell TEM data. On this basis, we identify the structure−function link in the RCL nanoparticles to be the unusually well-dispersed multicore structure that leads to their strong heating capability. This insight provides an important design characteristic for the future development of bespoke nanomaterials for this significant clinical application.

KEYWORDS: in situ TEM, liquid-phase TEM, cryo-TEM, magnetic nanoparticles, magnetic hyperthermia
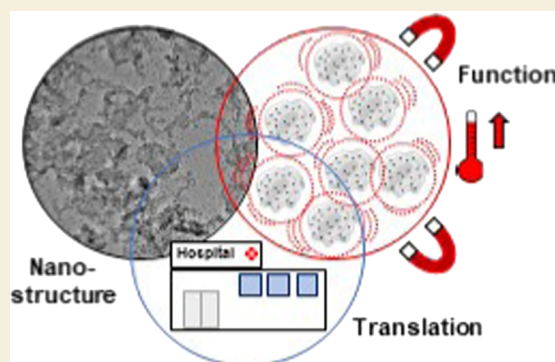
■ INTRODUCTION

A precise characterization of nanomaterials is crucial to fully understand their functional properties. Transmission electron microscopy (TEM) is a powerful technique for structural study at the atomic scale.[1] However, conventional techniques of TEM are limited to vacuum-dried samples, the dehydration of which often alters the state or induces artifacts. In the case of nanoparticles in solution, an alternative modality is cryogenic TEM (cryo-TEM),[2,3] in which the entire sample is frozen so that the supernatant fluid is retained, albeit in an altered state. Recently, the use of liquid-phase TEM has enabled *in situ* imaging of nanoparticles dispersed in fluids in their native environment.[4,5] Liquid-phase TEM offers direct real-space, real-time imaging of structural and functional dynamics in a native liquid environment with nanometer resolution. It shows huge potential for use in the characterization of materials in solution or solid−liquid dispersions, especially in the field of nanomedicine, where nanoparticles intended for use in biological media are often in solution.

Among various solid−liquid dispersions that are of interest in nanomedicine, magnetic fluids are of particular importance. These fluids, which comprise suspensions of magnetic nanoparticles (MNPs) in biocompatible media, have been studied for at least 20 years in relation to a wide range of potential biomedical and clinical applications.[6−8] A substantial amount of interest currently surrounds their use in cancer therapies, and in particular, in magnetic thermotherapy.[6,9] Certain MNPs generate significant heat when exposed to time-varying magnetic fields at appropriately tuned frequencies and amplitudes.[9] A case in point is a magnetic fluid, manufactured by Resonant Circuits Limited (RCL), U.K., which is currently being used in a clinical

study at Vall d'Hebron Barcelona Hospital on the thermotherapeutic treatment of locally advanced pancreatic cancer.[10,11] The RCL suite of magnetic fluids—known variously as "RCL-XX", "RCL-01", "RCL Agent", and "NTT Agent"—differ only in the excipient formulation. All contain the same solid matter part, referred to here as "the RCL nanoparticles". These are multicore MNPs, meaning that they fall into a class of materials defined as those nanoparticles containing more than one magnetic core (this could be an individual nanoscale crystallite or polycrystalline object formed of magnetic material) that are physically distinguishable due to being embedded in a nonmagnetic matrix that physically separates each core from its neighbor or neighbors.[12] In the RCL nanoparticles, the magnetic cores comprise iron oxide in the form of magnetite, Fe_3O_4, and/or maghemite, $\gamma\text{-}Fe_2O_3$, and the nonmagnetic matrix is a low-molecular-weight (ca. 40 kDa) polysaccharide dextran H-$(C_6H_{10}O_5)_xOH$.

The RCL nanoparticles are very effective magnetic heating materials. Their intrinsic loss power (ILP) is ca. 5.0 nHm^2/kg_{Fe}, which is 60% higher than that of the best-performing MNPs approved for clinical use, Resovist.[13] Under the time-varying magnetic field conditions being employed in the Barcelona clinical study[11] (amplitude $H_0 \cong 4$ kAm^{-1}, frequency $f \cong 300$ kHz), the rate of energy dissipation into the particles (known as the specific loss power, SLP) is ca. 24 mW/mg_{Fe}. For the patients in that study, where the 0.5 mL injected dose of magnetic fluid contains ca. 37.5 mg_{Fe}, which is expected to disperse over ca. 1.5 mL of tumor tissue, the estimated thermal dose (known as the specific absorption rate, SAR) is ca. 600 mW/g_{tissue} (assuming 100% retention of the injected material).

Such high ILP heating metrics shown by the RCL nanoparticles may reasonably be attributed to an optimal assembly of their internal multicore structure. This hypothesized correlation between structural and functional properties has been considered by several groups, all of them postulating that a key factor determining the magnetic heating capacity is the strength of the internal core−core (dipolar) magnetic interactions.[6,14−16] In perhaps the best experimental test of this hypothesis to date,[15] in a series of multicore particles made under controlled synthesis conditions wherein the core−core interaction field strength H_{int} (as measured by bulk magnetometry) was systematically varied, it was found that the particles with the weaker H_{int} (in the range 3.2 to 6.4 kA/m) exhibited the higher ILP values (in the range of 3 to 4 nHm^2/kg_{Fe}), with the larger ILP being associated with the lower H_{int}. It was also determined that the H_{int} interactions were demagnetizing in nature, and acting to hinder the magnetic heating mechanism, thereby adding a further logical explanation for the origin of the functional effect.[15]

However, to date, there have not been any comprehensive imaging studies performed on best-in-class multicore MNPs for magnetic heating with regard to their internal structural, morphological, and topological properties. To address this gap in knowledge, we have investigated the structural properties of the RCL nanoparticles using conventional TEM, high-resolution TEM (HRTEM), bright-field scanning TEM (BF-STEM), high-angle annular dark-field scanning TEM (HAADF-STEM), cryo-TEM, and liquid-phase TEM techniques. To guard against possible methodological artifacts, for example, those associated with sample preparation methods, we have performed completely independent cryo-TEM studies at three different laboratories in France (Marseille), Italy (Pavia), and Germany (Jena); and to investigate possible batchwise

variations or aging effects we have used samples from two separate manufacturing batches, ranging from ca. 15 to 25 months old at the time of measurement.

Alongside this insight into the structural origins of the RCL nanoparticles, this study highlights the usefulness of liquid-phase *in situ* TEM for ruling out artifacts related to sample preparation when studying nanomaterials intended for use as a solution.

■ EXPERIMENTAL METHODS

Materials

Two samples containing RCL nanoparticles were provided by Resonant Circuits Limited for TEM analyses; one was manufactured in 2017 and one in 2019. Both comprised a dispersion of multicore MNPs in an isotonic solution of water for injection and saline. Both were supplied sterile in glass vials containing 0.5 mL of the product. The constituent dextran-coated iron oxide nanoparticles were formed as a result of a reaction, at ca. 65 °C, of pharmaceutical-grade iron salts and low-molecular-weight (40 kDa) dextran, mediated by the addition of a reducing agent. One vial of the first sample, denoted RCL-01/2017 (ref RCL2001; lot no. 2017-319), was supplied to the research team in Jena. Separate vials of the second sample, denoted RCL-XX/2021 (ref RCL2001; lot no. 2021-307.1), were supplied to the research teams in Marseille and Pavia.

According to the manufacturer, the postproduction shelf life for both samples was 60 months, against the following product specifications: mean particle diameter (Z-average) 100 to 160 nm; polydispersity index <0.30; solid matter concentration 150 to 250 mg/mL; osmolality 250 to 350 $mOsmol/kg_{Fe}$; iron concentration 70 to 80 mg_{Fe}/mL; endotoxin concentration <0.5 EU/mL; micro-organism contamination <100 cfu/mL; and intrinsic loss power ≥5.0 nHm^2/kg_{Fe}. It should be noted that all of these are macroscopic parameters that may not be significantly affected by changes in the microstructure of the RCL nanoparticles and that the long shelf life does not preclude the possibility that some aging-related effects might be observable in the TEM experiments. With this in mind, it is noted that the sample ages at the time of measurement were as follows: Jena, ca. 15 months; Pavia, ca. 19 months; and Marseille, ca. 25 months.

A third sample, manufactured in 2023 and denoted as RCL-XX/2023 (ref RCL2001; lot no. 2023-191), was used in the magnetic interaction field analysis.

Physicochemical Characterization

The physicochemical properties of the RCL-01/2017 and RCL-XX/2021 samples, as reported by the manufacturer, were as follows. The product comprised "magnetic dextran iron oxide nanoparticles in water for injection with saline". The iron oxide was an unspecified combination of magnetite (Fe_3O_4, CAS: 1317-61-9) and/or maghemite ($\gamma\text{-}Fe_2O_3$, CAS: 1309-37-1), while the dextran was specified as $H(C_6H_{10}O_5)_xOH$ (CAS: 9004-54-0) with a molecular weight of 40 kDa. The mean Z-average hydrodynamic diameter of the nanoparticles was 149 nm for RCL-01, and 139 nm for RCL-XX, as determined by photon correlation spectroscopy (PCS) according to DIN ISO 13321 with a Zetasizer NanoZS90 instrument (Malvern Instruments Ltd., U.K.), against a NIST-traceable size standard. The associated polydispersity indices of 0.26 and 0.23 respectively were determined by the same PCS measurement. The solid matter concentrations were 188 and 197 mg/mL respectively, as measured in triplicate by the gravimetric method. The iron concentrations were 72.0 and 75.2 mg_{Fe}/mL respectively, as determined by spectrophotometry against a Titrisol iron standard (Merck KGaA, Germany). The intrinsic loss powers (ILP) were 5.1 and 5.0 nHm^2/kg_{Fe}, respectively, as measured using a Benchtop MACH System (Resonant Circuits Limited, U.K.), and following the protocol specified in that instrument's instructions for use.

Transmission Electron Microscopy

In Marseille: all the observations in standard, STEM, and liquid-phase TEM were performed with a JEOL 2100 electron microscope working at 200 kV. STEM HAADF characterizations were performed using a
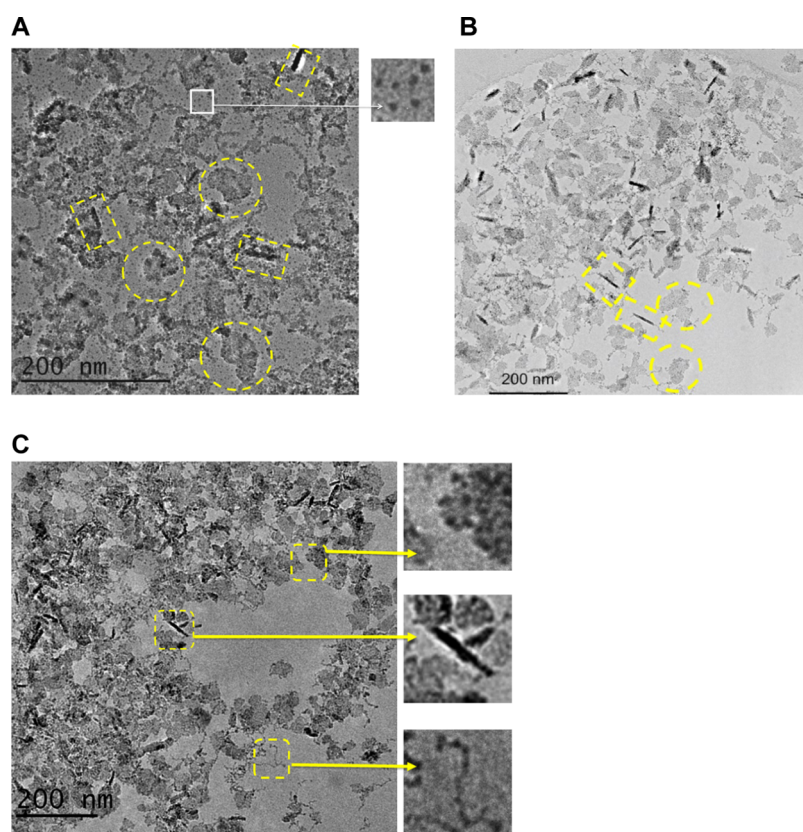
Figure 1. Multimodality TEM images of the RCL nanoparticles, for samples from the same as-supplied vial of the material. (A) Conventional TEM image of the sample after drying on a microscopy grid, with hydrated dextran lamellae highlighted in dashed circles; nanorods highlighted in dashed rectangles; and grid-deposited iron oxide cores highlighted in the expanded box. (B) Cryo-TEM image of the sample in a vitrified ice well, with dextran lamellae and nanorods highlighted in dashed circles and rectangles, respectively. (C) Liquid-phase TEM image of the sample, with lamellae, nanorods, and chain-like features highlighted in the expanded boxes.

nominal probe size of 0.5 nm, and inner and outer collection angles were 70 and 186 mrad. Liquid-phase TEM observations used a commercial PROTOCHIPS sample holder, type Poseidon, able to work in static conditions or under liquid flow, at a controlled temperature below 100 °C, with a spacer between the Si_3N_4 membranes between 20 and 150 nm. Experiments were performed under static conditions, with a 150 nm thick spacer. Irradiation at the sample level was maintained at 928 Cs^{-1} m^{-2} to limit possible radiolysis artifacts due to the electron beam, such as induced crystallization. For this purpose, magnification was limited in the range from ×20,000 to ×50,000. For the cryo-TEM measurements, 4.0 μL of the sample (diluted 100 times from the vial solution) was deposited on glow-discharged holey carbon grids (C-Flat 1.2/1.3) and vitrified using a Vitrobot (Thermo Fisher Scientific). Micrographs were recorded on a Tecnai electron microscope (Thermo Fisher Scientific) at 200 kV and at a nominal magnification of ×67,400 with a CMOS camera (Oneview Gatan).

In Pavia: cryogenic experiments were performed on a Glacios (Thermo Fisher Scientific) TEM equipped with a 200 kV high-tension generator, X-FEG electron source, liquid nitrogen cooling, sample autoloader, CMOS detector (Ceta 16 M Camera), and direct electron detector (Falcon 3EC). Satellite instrumentation (in a separate room) included a cooling unit and network PC for data storage. A Vitrobot (Thermo Fisher Scientific) device was used for PC-controlled vitrification of aqueous samples.

In Jena: for the recording of a tomographic TEM tilt-series of images, an EM grid with particles was placed in a tilt-rotate specimen holder (Model 626; Gatan Pleasanton). The data set was recorded using a CM120 cryo-transmission electron microscope (FEI, Eindhoven, Netherlands) operated at 120 kV. Images were captured and aligned every 2° over a 0 to +30° range using a 2 K CMOS Camera (F216, software EMMENU V4.0; camera and software TVIPS, Munich,

Germany). The tilt-series images were merged into a 1 fps video file using the open-source Image-J software.

Magnetic Characterization

The core−core interaction field strength H_{int} was determined for the RCL-XX/2023 nanoparticles using the Henkel-plot method as described in detail elsewhere.[15,17−19] Samples were prepared by air-drying aliquots of the magnetic fluid deposited onto zero background cotton wool. Isothermal remanent magnetization (IRM) and direct current demagnetization (DCD) measurements were carried out using a Quantum Design hybrid superconducting quantum interference device vibrating sample magnetometer (SQUID-VSM) at 5 K, with applied fields up to 5.6 MA/m. The IRM curve here is obtained by sequentially cycling the applied field from zero to +H and back to zero until a saturated state is reached for which increasing H no longer changes the measured remanent magnetization. The DCD curve is then obtained by reversing the direction of the applied field and measuring the remanent magnetization after sequential cycling of the field from zero to −H and back to zero until the reverse-saturated state is reached. The mean interaction field in the system is then defined to be $H_{int} = 1/2$ $|H_{r'} − H_{d'}|$, where $H_{r'}$ and $H_{d'}$ correspond to the positions of the maxima of the field derivatives of the IRM and DCD curves, respectively.

■ RESULTS

TEM data were recorded for two different samples at three different sites: RCL-01/2017 in Jena, and RCL-XX/2021 in Pavia and Marseille. In the following, unless stated otherwise, we focus on the TEM data generated in Marseille, the site of the most comprehensive set of experiments. Representative TEM data from the Pavia and Jena sites are provided in the Supporting Information S1 and S2 respectively.

Multimodality TEM Indicates Dextran Lamellae and Nanorods, and Iron Oxide Cores

We first examined the size, morphology, and structure of the RCL nanoparticles using conventional TEM, with a sample prepared by drying on a microscopy grid (see Figure 1A). The most common features seen in the image, highlighted in dashed circles in the figure, are irregular lamellae of lateral dimensions of ca. 30 to 90 nm and small but indeterminate thickness. (In-plane settling made accurate estimation of the latter impossible.) A thin lamellar morphology is typical of linear polysaccharides like dextran,[20] which can have lateral dimensions up to several microns and be only one to a few tens of nanometers thick. This morphology is partly a consequence of the structure of the crystalline forms of simple linear polysaccharides, wherein the polymer chain axis lies normal to the lamellar plane.[20] Some elongated rod- or lath-shaped features—which we shall refer to as "nanorods"—are also visible in the image (highlighted in dashed rectangles), these being of length ca. 30 to 60 nm and width ca. 6 to 14 nm. They are more electron-dense than the lamellae, and appear darker in the images; however, from the conventional TEM alone, their origin is not clear.

Also visible in Figure 1A, over the entire surface of the grid, on or within both the lamellae and the nanorods, and on the grid itself (highlighted in the expanded box), are numerous small and uniform circular features with diameters of 3.7 nm (mean) ± 0.6 nm (standard deviation). Given their shape and high electron density, we attribute these to the expected iron oxide cores in the sample, which typically crystallize as approximately spherical objects.[21] It is not clear from this experiment alone whether the uniform dispersion of the cores is an artifact of the drying process (e.g., that the cores might have become detached or dislodged during drying, and thereafter dispersed over the grid) or a true reflection of the sample morphology (e.g., that the cores might naturally be present in the supernatant fluid, rather than associated with dextran *per se*).

Next, we performed cryo-TEM to visualize the samples in an almost frozen native environment (see Figure 1B and the Supporting Information S1 and S2 for the data collected in Marseille, Pavia, and Jena). Again, the most common objects are the dextran lamellae (highlighted in dashed circles in Figure 1B), along with the less common nanorods (highlighted in dashed rectangles). Noticeably different from the conventional TEM image, however, is the distribution of iron oxide cores: viz., there is no evidence of any isolated iron oxide cores dispersed in the sample. This implies that the isolated iron oxide cores seen in the conventional TEM image in Figure 1A were artifacts of the sample preparation due to the obligatory drying process. That said, on close inspection, it is possible to discern some occasional chain-like structures adjacent to the lamellae and nanorods which might plausibly be chains of weakly coupled (via dipole—dipole interactions) cores that remain intact in cryo-TEM but which are dispersed onto the microscopy grid under the drying conditions of conventional TEM.

In Marseille, we also performed liquid-phase TEM, thereby enabling true *in situ* TEM of the RCL nanoparticles in their native environment, viz. dispersed in a fluid. As can be seen in Figure 1C, the liquid-phase TEM confirms the findings of cryo-TEM, with the same lamellae and nanorod features being evident, and with the iron oxide cores occurring only within or on those features. Also echoing the cryo-TEM results, occasional "nanoribbon" features (highlighted in the expanded box) can be seen. These have an electron density commensurate with their being made from chains of iron oxide cores.

Despite the presence of occasional nanoribbon features in the cryo- and liquid-TEM images, it is notable that a large majority of iron oxide cores are embedded in or attached to the dextran lamellae and the nanorods. In the case of lamellae, it is also clear that the iron oxide cores are spatially well distributed and separated from one another, in a manner that is quite unusual for multicore nanoparticles, where it is common to observe clusters of cores embedded within the encompassing matrix.[22]

It is also interesting to note across all three TEM modalities that the underlying sizes of the lamellae and nanorod features are similar, and that they are significantly less than the manufacturer-reported 139 nm Z-averaged mean hydrodynamic diameter of the RCL nanoparticles, a parameter that was measured by photocorrelation spectroscopy (PCS). However, it is also clear from the TEM images that the lamellae and nanorods seem to preferentially form aggregated assemblies rather than exist as separate entities in the supernatant fluid, which may account for the larger size recorded by PCS.

Electron Tomography of the Nanorods is Different in Cryogenic and Dried Samples

A further interesting point is that all three modalities feature the nanorods as well as the lamellae and that they appear in similar proportions in all three modalities. To quantify this, the numerical ratio of lamellae to nanorods was determined by visual inspection of single images. For conventional TEM, this yielded the ratio 93/17 from $N = 110$ objects inspected; for cryo-TEM it was 137/25 from $N = 162$ objects; and for liquid-phase TEM it was 137/23 from $N = 160$ objects. Therefore, in all three modalities, ca. 85% of the identified objects were classified as lamellae, and ca. 15% were classified as nanorods.

We postulate four possible interpretations/explanations of the origin and nature of the nanorods. (a) One possibility is that they are "edge-on" lamellae, i.e., lamellae for which the normal to the lamellar plane (the crystallographic *c*-axis) happens to lie in or close to the plane perpendicular to the electron beam axis. If this were the case, then the spread in observed widths and electron densities of the nanorods in the TEM images could be interpreted as variations in the angle of incidence between the beam and the *c* axis. (b) A different explanation is that the nanorods are an entirely separate material phase. It may be noted here that dextran is known to crystallize into two different polymorphs: a hydrated form, which has a flat lozenge morphology and is synthesized at temperatures below 100 °C;[23,24] and an anhydrous form, which has a lath-shaped morphology and is synthesized at higher temperatures, 120 to 200 °C.[25] Although the nanorods could be regarded as lath-shaped, this explanation seems unlikely given that the RCL nanoparticles are synthesized at 60 to 65 °C; however, it might be an indication of a possible destination phase for the sample, under certain conditions. (c) A third possibility is that the nanorods might correspond to the initial stages of the growth of the low-temperature, hydrated dextran lamellae, which has previously been identified as having a lath-shaped morphology.[24] However, if this were the case, then the observed spread in electron densities of the nanorods is difficult to understand, as one would then expect the nanorods to be of a similar thickness to the lamellae. (d) A fourth hypothesis is a variation of the first, differing only in relation to the dried-sample state in conventional TEM. In this case, the nanorods are again "edge-on" lamellae, however, during drying, they collapse or concertina into a more condensed, flattened feature on the sample plane. Such a collapse would imply that the lamellae are structurally
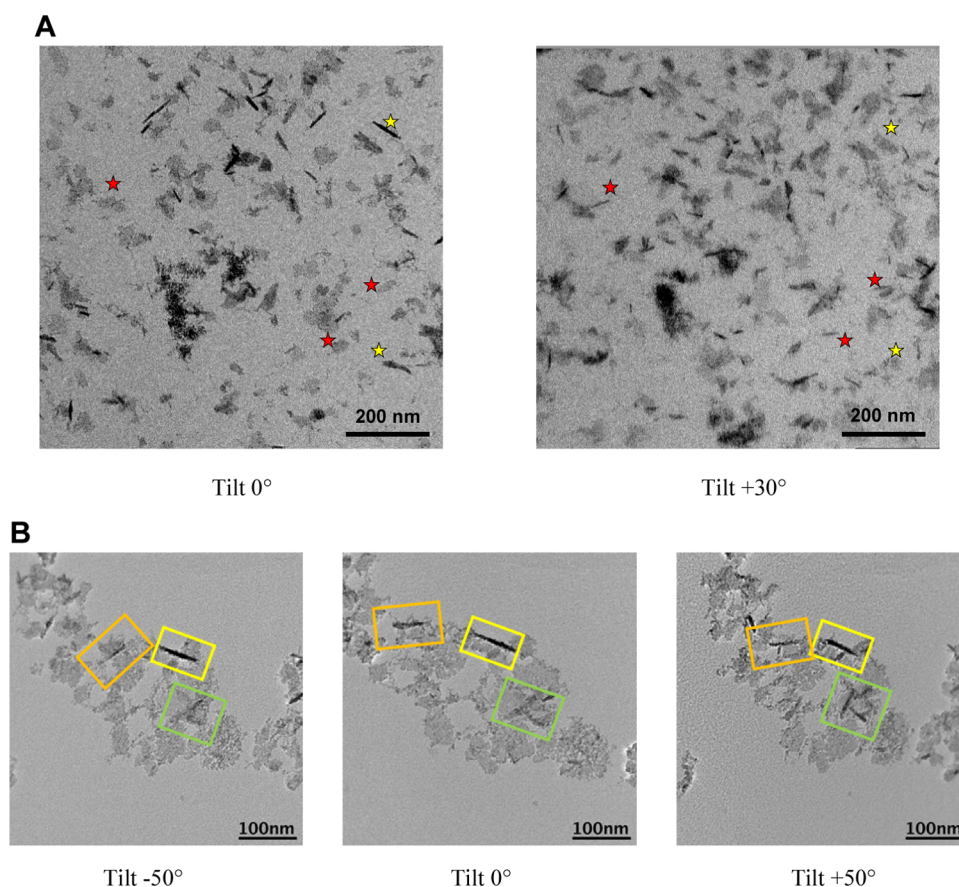
Figure 2. Selected TEM images of the RCL nanoparticles from tilt-series recordings at different angles of incidence between the electron beam and the normal to the sample plane. (A) Cryo-TEM images recorded in Jena on sample RCL-01/2017. The features highlighted with yellow (and red) stars indicate lamella to nanorod (and vice versa) transformations as the tilt angle is increased. (B) Conventional dried-sample TEM images recorded in Marseille on sample RCL-XX/2021. In this case, the nanorod features, highlighted in solid rectangles, are largely impervious to the change in the tilt angle.
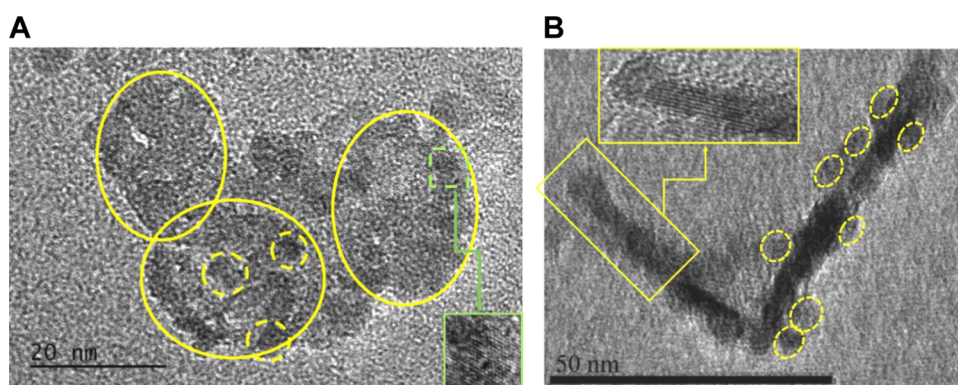

Figure 3. Dried-sample HRTEM images of RCL nanoparticles. (A) Image of a single polycrystalline hydrated dextran lamella, with component monocrystalline parts (evidenced by lattice fringes) highlighted in solid ellipses. The image also contains iron oxide cores, including those highlighted in dashed circles. The inset is an enlargement of the iron oxide core highlighted in the dashed square: the lattice spacings of 0.48 nm are consistent with the (110) planes of magnetite or maghemite. (B) Image of two monocrystalline hydrated dextran nanorods with associated iron oxide cores highlighted in dashed ellipses.
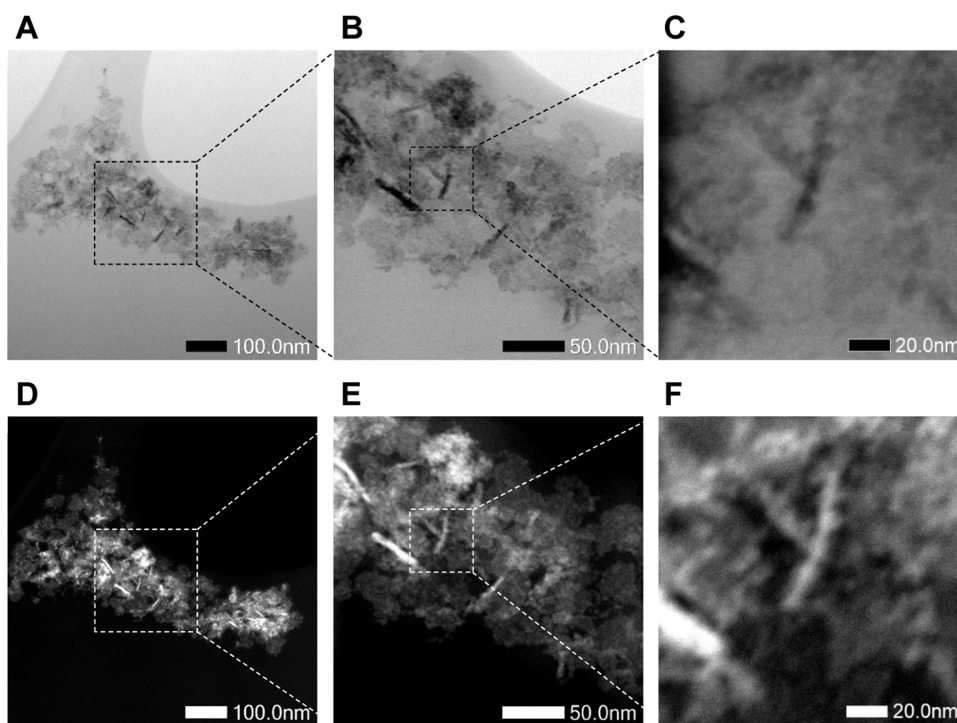
fragile, to allow such a deformation—which is feasible, given that they are very thin, and not particularly well crystallized.

To explore further the nanorods, three-dimensional (3D) tomographic TEM experiments were performed in both Jena (cryo-TEM, on the RCL-01/2017 sample) and in Marseille (conventional dried-sample TEM, on the RCL-XX/2021 sample) by tilting the imaging plane of the microscope relative to the electron beam direction. The results of these studies are summarized in Figure 2; further images at intermediate tilt angles are provided in the Supporting Information S2 and Video S1. Figure 2A shows the cryo-TEM results from Jena for the tilt angles[1] $\theta = 0$ and $+30°$; Figure 2B shows the conventional TEM data from Marseille at tilt angles $\theta = -50, 0,$ and $+50°$.
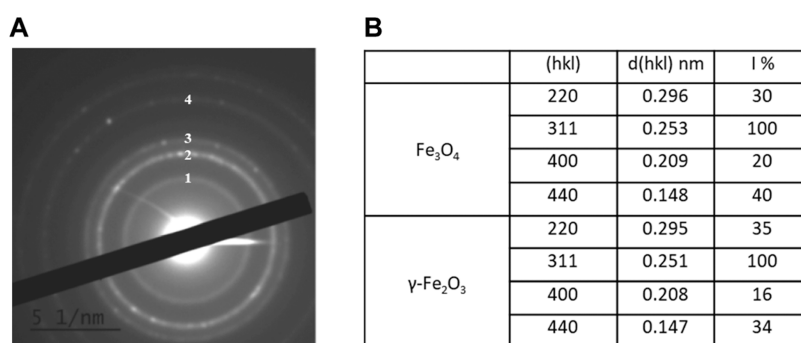
Figure 4. Electron diffraction data for the iron oxide cores in the RCL nanoparticles. (A) Diffraction pattern, with the visible rings corresponding to the magnetite (Fe_3O_4) and/or maghemite (γ-Fe_2O_3) cores: 1st ring: d(220); 2nd ring: d(311); 3rd ring: d(400); 4th ring: d(440). (B) Reference data for magnetite and maghemite: h, k, and l are Miller indices denoting the intercept of the plane with the x-, y-, and z-axis respectively; d(hkl) is the distance between adjacent crystallographic planes in nanometers; and I (%) is the intensity as a percentage of the strongest diffraction peak.

	(hkl)	d(hkl) nm	I %
Fe_3O_4	220	0.296	30
	311	0.253	100
	400	0.209	20
	440	0.148	40
γ-Fe_2O_3	220	0.295	35
	311	0.251	100
	400	0.208	16
	440	0.147	34

Figure 5. Dried-sample STEM images of the RCL nanoparticles in BF (phase contrast) and HAADF (chemical contrast) modes, highlighting the spatial distribution of the iron oxide cores. (A−C) BF-STEM images with increasing magnification showing the coexistence of lamellae and nanorods. (D−F) The same images obtained using HAADF-STEM show that the cores are present in or on both the lamellae and the nanorods, but for the nanorods the core-to-core separation distance is smaller than that for the lamellae, as evidenced by the higher contrast.

On inspection of the Jena data in Figure 2A, there appears to be strong evidence in favor of some nanorods in the initial orientation image transforming to lamellae in the +30° image (highlighted with yellow stars), and some lamellae transforming into nanorods (highlighted with red stars). This observation supports the hypothesis that the nanorod features are edge-on lamellae. In contrast, in the Marseille data in Figure 2B, there appears to be strong evidence in favor of some nanorods (highlighted in rectangles) being rod- or lath-shaped objects, given that their appearance does not significantly change over the entire tilt angle range from −50 to +50°. This observation potentially supports the hypotheses that the nanorods are either a separate material phase, or the lath-shaped initial growth phase of the lamellae, or a drying-induced collapse of edge-on lamellae.

In light of the electron tomography results, additional dried-sample TEM experiments − HRTEM, electron diffraction, BF-STEM, and HAADF-STEM − were undertaken in Marseille to probe further the structure and crystallinity of the dextran and cores, and also the spatial distribution of the cores.

Dextran Crystallizes in the Low-Temperature Hydrated Polymorph; Cores are Monocrystalline Magnetite and/or Maghemite

Lattice fringes evident in the HRTEM images indicate that the irregularly shaped dextran lamellae are polycrystalline—a representative example of this is shown in Figure 3A—and that the iron oxide cores are monocrystalline. Many crystallographic orientations are possible between the lattices of the cores and the dextran. Some cores are also observed in the top view along the c-axis with the lattice planes aligned with the lattice of the dextran matrix. The core highlighted in the inset in Figure 3A has lattice spacings of ca. 0.48 nm, which is consistent with the (110) planes of magnetite or maghemite.
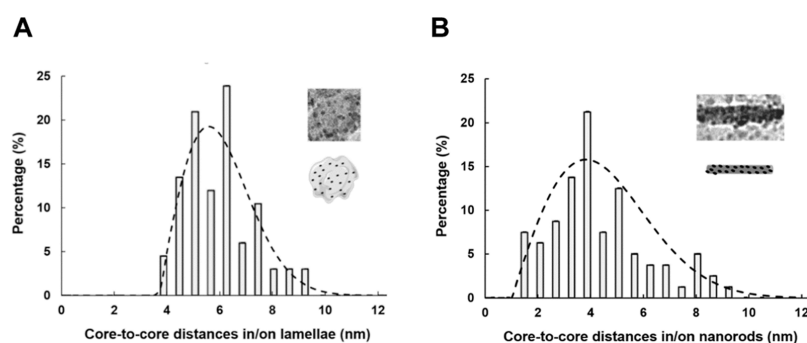
Figure 6. Histograms of the measured in-plane core-to-core separation distances of neighboring iron oxide cores in and/or on: (A) the dextran lamellae; and (B) the dextran nanorods. The dashed line curves superimposed on both histograms are guides to the eye based on modified forms of the two-dimensional γ function, as described in the text. The insets show enlarged liquid-phase TEM images of a lamella and a nanorod respectively (image scale: horizontal size = 50 nm); and cartoon drawings of the same, highlighting the well-dispersed distributions of the cores in/on the dextran.

Well-resolved lattice fringes were observed in the HRTEM images of some of the nanorods (Figure 3B). On inspection, it was found that these fringes were consistent with the monoclinic structure of the low-temperature hydrated polymorph of dextran ($a = 2.571$ nm, $b = 1.021$ nm, $c = 0.776$ nm, $\beta = 91.3°$).[24] The measured spacings between the fringes in the elongated direction ($d = 0.479$ nm, highlighted in the inset in Figure 3B) can be attributed to the (220) lattice planes of hydrated dextran. Many iron oxide cores can be observed attached to the surfaces of these nanorods.

To further investigate the crystalline structures, we next performed electron diffraction and measured the visible rings in the diffraction patterns (Figure 4A). On inspection, it was found that the rings were dominated by reflections from the electron-dense iron oxide cores. The electron diffracted intensity of the hydrated dextran matrix is low compared to the diffraction from iron oxide, so in our work, the crystallinity of the support is better studied from the HRTEM images, which also indicate the dimensions of the grains in the polycrystalline lamellae (Figure 3A). Four main rings are visible (see Figure 4B), all of which are consistent with those expected from either magnetite or maghemite. (The resolution was not sufficient to distinguish between the two.) All of the rings were continuous and diffuse, as expected given the random relative orientation and small size of the iron oxide cores (ca. 3.7 nm) obtained by direct measurements on the HRTEM images. In some cases, the rings also contained separated spots superimposed thereon—see, for example, the second ring in Figure 4A − indicating particularly strong reflections from some cores.

Core-to-Core Distances are Larger for Lamellae than for Nanorods

The observed contrast in the TEM images arises both from the electron absorption in the sample and from the Bragg orientation of the crystalline parts of the sample. To separate these contributions, we next performed both bright-field scanning TEM (BF-STEM, Figure 5A−C) to study phase contrast, and high-angle annular dark-field scanning TEM (HAADF-STEM, Figure 5D−F) to study chemical contrast, in the sample. These imaging modes are useful as we expect the large atomic number of the Fe in the cores to promote more electron scattering at larger angles (leading to brighter regions), while the lighter elements in the dextran should scatter electrons at smaller angles (resulting in darker regions) − which we can use to probe the spatial distribution of the iron oxide cores.[6]

Figure 5 shows BF-STEM and HAADF-STEM images, at increasing magnifications, of the same section of a dried sample.

On inspection, it appears that the iron oxide cores are embedded in or attached to both the dextran lamellae and the nanorods, but that they are spatially more concentrated in/on the nanorods, as evidenced by the higher image contrast (darker in the BF images, lighter in the HAADF images) of the nanorods, compared to the lamellae. Such differences in core-to-core distances may also explain the contrast differences seen in earlier TEM images such as those in Figure 1.

Distribution of Core-to-Core Distances is Consistent with Uniform Disaggregation

To further explore the spatial distribution of the cores, we inspected and analyzed the best available liquid-phase TEM images to build up histograms of core-to-core distances in and/or on isolated lamellae and nanorods. To do this a single core within a lamella or nanorod was selected, and an origin point was set at its center; then, by scanning at around 360° in the plane of the image, all the first-neighbor cores were identified. For each of these first-neighbor cores, the center was located, and the origin-to-core-center distance was recorded. These data were then transformed into a histogram of core-to-core distances with a box width of 0.6 nm, as shown in Figure 6. For the lamellae (Figure 6A): 67 pairs were identified, with minimum, median, and maximum core-to-core distances of 3.92, 5.98, and 9.51 nm, respectively. For the nanorods (Figure 6B): 80 pairs were identified, with minimum, median, and maximum core-to-core distances of 1.43, 3.97, and 9.26 nm, respectively.

Although the quantity of data collected was not sufficient to allow definitive quantitative analysis of the distributions, we decided nonetheless to compare the observations with the predicted two-dimensional γ probability distribution, $P(r) \propto r \exp[-\sigma\pi r^2]$, for the distances r between a randomly selected point on a plane and a collection of randomly distributed reference points on the same plane, for a given areal density σ of reference points.[26] On inspection, it was found that both of the histograms in Figure 6 are reasonably consistent with the γ distribution interpretation, but only if an offset transformation was applied, so that $P(r) = 0$ for $r < r_0$, and $P(r) \propto (r - r_0)\exp[-\sigma\pi(r - r_0)^2]$ for $r \geq r_0$. The dashed curves in Figure 6 were manually adjusted to these forms: for the lamellae in Figure 6A, $r_0 = 3.7$ nm and $\sigma = 0.045$ nm^{-2}; and for the nanorods in Figure 6B, $r_0 = 1.0$ nm and $\sigma = 0.020$ nm^{-2}. The smaller r_0 in the nanorods distribution is consistent with a higher spatial concentration of cores, as observed in Figures 1 and 5. The smaller σ (and therefore broader distribution) in the nanorods is somewhat counterintuitive but is consistent with the nanorods in the liquid-sample TEM being edge-on lamellae, which would
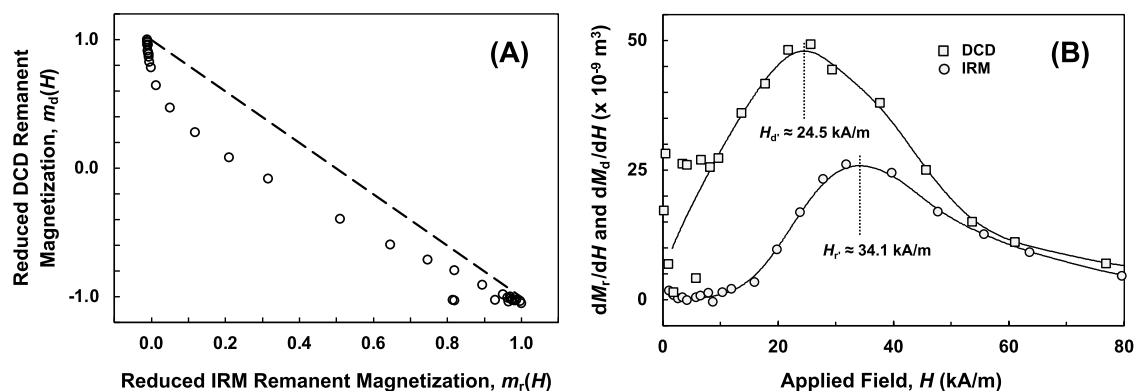
Figure 7. Magnetic characterization of the core−core interactions in the RCL nanoparticles. (A) Henkel plot of the remanent magnetization $m_d(H) = M_d(H)/M_d(H_{max})$ from direct current demagnetization (DCD) runs as a function of $m_r(H) = M_r(H)/M_r(H_{max})$ from isothermal remanent magnetization (IRM) runs, as measured at 5 K. The excursion of the data points below the noninteracting Wohlfarth relationship line (the dashed line) signifies that demagnetizing core−core interactions are present. (B) Gradient dM_r/dH and dM_d/dH curves derived from the IRM and DCD and IRM data at 5 K. The mean core−core interaction field, $H_{int} = 1/2 |H_{r'} - H_{d'}| \approx 4.8$ kA/m, where, as indicated, $H_{r'}$ and $H_{d'}$ correspond to the applied field values at the maxima of the derivative IRM and DCD curves, respectively.

skew the distribution toward smaller r values. The nonzero r_0 in both the lamellae and nanorods, coupled with the observation that in the lamellae the minimum recorded core-to-core distance of 3.92 nm was greater than the mean 3.7 nm diameter of the cores, indicates a largely uniform disaggregation (i.e., absence of agglomeration) of the cores in the RCL nanoparticles.

To complete the TEM studies, we also attempted to estimate the average number of cores on or in each lamella or nanorod. The high prevalence of overlapping lamellae made this difficult, to the extent that we were unable to reach a reliable conclusion. That said, it was our impression that both the lamellae and the nanorods were typically associated with tens of iron oxide cores.

Henkel-Plot Data Indicates a Weak, Demagnetizing Core−Core Interaction Field

Lastly, to relate more directly to the observed physical and functional properties of the RCL nanoparticles, the mean core−core interaction field strength H_{int} was determined for the RCL-XX/2023 sample using the Henkel-plot method.[15,17−19] Figure 7A shows the Henkel plot obtained at 5 K following a series of isothermal remanent magnetization (IRM) and direct current demagnetization (DCD) measurements, recorded using the methodology described in the Experimental Methods Section. Further details on these data are provided in the Supporting Information S3.

As is customary in Henkel plots, the reduced remanent magnetizations—$m_r(H) = M_r(H)/M_r(H_{max})$ from the IRM runs, with values ranging from 0 to +1, and $m_d(H) = M_d(H)/M_d(H_{max})$ from the DCD runs, with values ranging from +1 to −1—are plotted against each other. In a system of non-interacting magnetic entities, the reduced IRM and DCD curves are expected to follow the Wohlfarth relationship:[27] $m_d(H) = 1 - 2m_r(H)$, so that a plot of $m_d(H)$ as a function of $m_r(H)$ is a straight line with slope −2, as shown as the dashed line in Figure 7A. Deviations from this line indicate either demagnetizing (below the line) or magnetizing (above the line) interactions. The Henkel data in Figure 7A fall below the Wohlfarth relationship line, indicating that demagnetizing core−core interactions are present.

We quantify these interactions using the interaction field, $H_{int} = 1/2|H_{r'} - H_{d'}|$, where $H_{r'}$ and $H_{d'}$ are the applied field values at the maxima of the derivatives of the $m_r(H)$ and $m_d(H)$ curves, respectively.[18,19] As shown in Figure 7B, $H_{r'} \approx 34.1$ kA/m and

$H_{d'} \approx 24.5$ kA/m; hence $H_{int} \approx 4.8$ kA/m. This is a weak field compared to those reported for other systems—e.g., $H_{int} \approx 30$ kA/m in core−shell iron/iron oxide nanoparticles[19] and $H_{int} \approx 95$ kA/m in nanocrystalline barium ferrites[18]—but it falls well within the 3.2 to 6.4 kA/m range reported for multicore iron oxide/citric-acid nanoparticles with strong magnetic heating properties (ILP values in the range 3 to 4 nHm²/kg$_{Fe}$).[15]

Previously there has not been sufficient knowledge of the internal structure of the multicore MNPs used in magnetic thermotherapy to enable a direct line to be drawn between their structural and functional properties. However, in this case, we have both the extensive TEM characterization data as well as the functional data relating to the high technical performance of the RCL nanoparticles, viz. an ILP of 5.1 nHm²/kg$_{Fe}$, and now the intrinsic metric of the mean core−core magnetic interaction field, $H_{int} \approx 4.8$ kA/m, which we can compare.

To do this we follow previous practice[18] by estimating the maximum dipolar field that a given iron oxide core would sense due to a nearest-neighbor core. Further details can be found in the Supporting Information S3, but in brief: assuming a point-dipole due to a single core of moment m_{sc}, the maximum dipolar field on a sphere surrounding the dipole will be along the dipole axis. At a distance r_{cc} from the magnetizing core, along that dipole axis, the dipolar field experienced by the nearest-neighbor core will be of magnitude $H_{d-max} = (2m_{sc})/(4\pi r_{cc}^3)$. From hysteresis data recorded at 5 K we know that the remanent magnetization in the RCL nanoparticle sample is ca. 50.8 Am²/kg$_{Fe}$. If we assume that the iron oxide cores are maghemite—a reasonable assumption given their small size and the likelihood of environmental oxidation of any magnetite that might have been present at synthesis[28]—of density 4.88 g/cm³, and that they are all of diameter 3.7 nm (from the TEM data), then we can estimate that for a single core, the remanent moment is $m_{sc} \approx 4.6 \times 10^{-21}$ Am². At $r_{cc} = 4$ nm, this gives a dipolar field $H_{d-max} = 11.4$ kA/m; at 5 nm it is 5.9 kA/m; and at 6 nm it is 3.4 kA/m. These estimates are comparable to the measured $H_{int} \approx 4.8$ kA/m in the RCL nanoparticles; indeed, we can obtain full agreement, with $H_{d-max} = 4.8$ kA/m, by setting $r_{cc} = 5.34$ nm.

It may be noted here that there are no free parameters in the H_{d-max} calculation, and that as such the close agreement between the $r_{cc} = 5.34$ nm value required for H_{d-max} to equal H_{int} and the actual core-to-core distances as measured in the RCL nano-particles (Figure 6) is a significant result. The implication is that

the high technical performance of the material for the thermotherapy application is related to the uniformly well-separated and unusually well-dispersed iron oxide cores in/on the dextran in the RCL nanoparticles, which accounts for the relatively weak (ca. 4.8 kA/m) demagnetizing interaction field acting between the cores.

◼ DISCUSSION AND CONCLUSIONS

We have structurally, morphologically, topologically, and magnetically characterized the RCL nanoparticles that are currently being used in a clinical study of thermotherapy to treat locally advanced pancreatic cancer. This was achieved using a combination of TEM techniques including HRTEM, cryo-TEM, HAADF-STEM, and liquid-phase TEM, plus advanced magnetic methods to probe the internal interactions in nanocomposite materials.

To guard against possible methodological artifacts, we performed completely independent cryo-TEM studies at three different laboratories in France (Marseille), Italy (Pavia), and Germany (Jena); and to investigate possible batchwise variations or aging effects we used samples from two separate manufacturing batches, ranging from ca. 15 to 25 months old at the time of measurement. No significant indications of site-specific bias, batchwise variation in sample characteristics, or aging effects, were noted in this respect.

Multimodality TEM imaging showed that the RCL nanoparticles mostly comprise irregularly shaped dextran lamellae of lateral dimensions of 30−90 nm and indeterminate thickness. All imaging modes also showed a distinct second component, accounting for ca. 15% n/n of the objects viewed, in the form of 30−60 nm long "nanorods", of unknown origin. A third component, in the form of well-dispersed ca. 3.7 nm diameter iron oxide cores, was observed in all the data, albeit in modality-dependent forms. In the cryogenic and liquid-sample images, these cores were observed to be either in or on the dextran lamellae and nanorods, or, occasionally, to form separate "nanoribbon" features, the latter most likely being loosely coupled chains of cores in the supernatant. In dried samples, the chain features were not observed, and instead isolated cores spread all over the sample plane, including the microscope grid itself, implying disaggregation of the nanoribbons on drying.

Cryogenic-sample electron tomography at tilt angles from 0 to +30° indicated that the nanorod features were dextran lamellae viewed "edge-on", but in dried samples, tomography at tilt angles from −50 to +50° were quite different, and instead indicated that the nanorods were rod- or lath-shaped forms. It was hypothesized that an explanation for this was that the dextran lamellae, being very thin, might be susceptible to drying-induced collapse onto the plane of the microscopy grid. HRTEM of dried samples showed that both the dextran lamellae and nanorods were crystallized in the monoclinic low-temperature hydrated dextran polymorph; and that the iron oxide cores were maghemite and/or magnetite monocrystals.

Both phase contrast and chemical contrast STEM imaging showed that the core-to-core distances were smaller in the nanorods than in the lamellae. This was confirmed by detailed scrutiny of isolated lamellae and nanorods across several liquid-phase TEM images, and this was used to build up histograms mapping the core-to-core distances in/on the nanoparticles. These histograms were of a form that was consistent with a γ distribution of nearest-neighbor distances in a plane randomly decorated with reference points, with the proviso that an offset was introduced to preclude the core-to-core distance falling to zero. It was also noted that in the lamellae the minimum recorded core-to-core distance exceeded the mean diameter of the cores, indicating that the cores in the nanoparticles are predominantly disaggregated and that there is an absence of core−core agglomeration in/on the dextran.

Magnetic remanence Henkel-plot analysis was performed at 5 K, which indicated that demagnetizing core−core interactions were present, with an interaction field of magnitude $H_{int} \approx 4.8$ kA/m. Theoretical estimates using a point-dipole model allowed a comparison to be made between H_{int} and the predicted field acting on a given iron oxide core assuming that it was collinear with another core that carried the remanent magnetization determined from macroscopic measurements on the RCL nanoparticles, and assuming a core diameter of 3.7 nm. It was found that for the predicted dipolar field to equal the measured H_{int} field, the core-to-core separation distance should be ca. 5 nm, which falls well within the ca. 4−6 nm range of separation distances observed in the liquid-cell TEM histogram data. We consider this to be a significant result that implies a direct connection between the structural properties of the RCL nanoparticles—in particular, the uniformly well-separated and unusually well-dispersed iron oxide cores and the associated ubiquitous but in this case relatively weak demagnetizing interaction between them—and their excellent magnetic heating properties.

In conclusion, we believe our findings have important implications for the development of multicore magnetic nanoparticles in thermotherapy. A better understanding of the structural morphology of such materials, including studies in their native liquid environment using advanced techniques such as liquid-phase TEM, is crucial to ensure the reliable development of these nanomaterials and their robust translation into clinical usage. We hope that our work here will encourage scientists to undertake similar detailed structural analyses of other multicore magnetic nanoparticles or other nanomaterials with the goal of better understanding the relationship between the structural and functional properties of these fascinating materials.

◼ ASSOCIATED CONTENT

Ⓢ🅘 Supporting Information

The Supporting Information is available free of charge at https://pubs.acs.org/doi/10.1021/acsmaterialsau.4c00021.

> Cryo-TEM data as collected in Pavia, Italy (S1); cryo-TEM data, including electron tomography data, as collected in Jena, Germany (S2); and magnetic characterization data and dipolar field modeling (S3) (PDF)

> RCL nanoparticles from cryo-TEM images tilted every 2° from 0 to +30° (video) (MP4)

◼ AUTHOR INFORMATION

Corresponding Authors

Quentin A. Pankhurst − *UCL Healthcare Biomagnetics Laboratory, University College London, London W1S 4BS, U.K.; Resonant Circuits Limited, London W1S 4BS, U.K.;* Email: q.pankhurst@ucl.ac.uk

Ling Peng − *Aix-Marseille Université, CNRS, Centre Interdisciplinaire de Nanoscience de Marseille, Equipe Labellisée Ligue Contre le Cancer, 13288 Marseille, France;* ⓞ orcid.org/0000-0003-3990-5248; Email: ling.peng@ univ-amu.fr

Suzanne Giorgio — *Aix-Marseille Université, CNRS, Centre Interdisciplinaire de Nanoscience de Marseille, Equipe Labellisée Ligue Contre le Cancer, 13288 Marseille, France*; Email: suzanne.giorgio@univ-amu.fr

Authors

Tom Roussel — *Aix-Marseille Université, CNRS, Centre Interdisciplinaire de Nanoscience de Marseille, Equipe Labellisée Ligue Contre le Cancer, 13288 Marseille, France*

Daniel Ferry — *Aix-Marseille Université, CNRS, Centre Interdisciplinaire de Nanoscience de Marseille, Equipe Labellisée Ligue Contre le Cancer, 13288 Marseille, France*

Artemis Kosta — *Aix-Marseille Université, CNRS, Institut de Microbiologie de la Méditerranée, 13009 Marseille, France*

Dalila Miele — *Department of Drug Sciences, University of Pavia, 27100 Pavia, Italy*

Giuseppina Sandri — *Department of Drug Sciences, University of Pavia, 27100 Pavia, Italy*

Felista L. Tansi — *Department of Experimental Radiology, Institute of Diagnostic and Interventional Radiology, Jena University Hospital—Friedrich Schiller University Jena, 07747 Jena, Germany*

Frank Steiniger — *Center for Electron Microscopy, Jena University Hospital—Friedrich Schiller University Jena, 07743 Jena, Germany*

Paul Southern — *UCL Healthcare Biomagnetics Laboratory, University College London, London W1S 4BS, U.K.; Resonant Circuits Limited, London W1S 4BS, U.K.*

Complete contact information is available at:
https://pubs.acs.org/10.1021/acsmaterialsau.4c00021

Author Contributions

T.R. was the principal author; T.R., A.K., D.M., G.S., F.L.T., and F.S. performed the conventional, cryo, and liquid-cell TEM experiments; D.F. performed the STEM HAADF analysis; P.S. performed the magnetic and calorimetric characterizations; and T.R., S.G., L.P., and Q.A.P. analyzed the data and wrote the manuscript. All authors have approved the final version of the manuscript. CRediT: **Tom Roussel** data curation, formal analysis, investigation, writing-original draft, writing-review & editing; **Daniel Ferry** data curation, formal analysis, investigation, methodology, writing-original draft, writing-review & editing; **Artemis Kosta** data curation; **Dalila Miele** data curation; **Giuseppina Sandri** data curation; **Felista Lemnyui Tansi** data curation, investigation; **Frank Steiniger** data curation, investigation; **Paul Southern** data curation, investigation; **Quentin Pankhurst** formal analysis, investigation, methodology, writing-review & editing; **Ling Peng** conceptualization, funding acquisition, project administration, supervision, writing-review & editing; **Suzanne Giorgio** conceptualization, data curation, formal analysis, investigation, methodology, supervision, writing-original draft, writing-review & editing.

Notes

The authors declare the following competing financial interest(s): During the project P.S. and Q.A.P. were employed in part by the company Resonant Circuits Limited. The remaining authors declare that the research was conducted in the absence of any commercial or financial relationships that could be construed as a potential conflict of interest.

ADDITIONAL NOTE

[1]The tilt angle θ is here defined with reference to a right-handed Cartesian coordinate system that is fixed relative to the sample plane. At $\theta = 0°$, the horizontal and vertical axes of the TEM image as recorded correspond to the x and y axes, respectively, both of which lie in the sample plane; and the electron beam is incident along the z-axis, which is normal to the sample plane. At a tilt angle of, for example, $\theta = +30°$, the sample is rotated clockwise about the y-axis by $30°$.

REFERENCES

(1) Li, G. X.; Zhang, H.; Han, Y. Applications of Transmission Electron Microscopy in Phase Engineering of Nanomaterials. *Chem. Rev.* **2023**, *123* (17), 10728−10749.

(2) Stewart, P. L. Cryo-electron Microscopy and Cryo-electron Tomography of Nanoparticles. *WIREs Nanomed. Nanobiotechnol.* **2017**, *9* (2), No. e1417, DOI: 10.1002/wnan.1417.

(3) Danino, D. Cryo-TEM of Soft Molecular Assemblies. *Curr. Opin. Colloid Interface Sci.* **2012**, *17* (6), 316−329.

(4) Sung, J.; Bae, Y.; Park, H.; Kang, S.; Choi, B. K.; Kim, J.; Park, J. Liquid-Phase Transmission Electron Microscopy for Reliable In Situ Imaging of Nanomaterials. *Annu. Rev. Chem. Biomol. Eng.* **2022**, *13*, 167−191.

(5) Ou, Z. H.; Liu, C.; Yao, L. H.; Chen, Q. Nanoscale Cinematography of Soft Matter System Under Liquid-Phase TEM. *Acc. Mater. Res.* **2020**, *1* (1), 41−52.

(6) Liu, Z.; Epicier, T.; Lefkir, Y.; Vitrant, G.; Destouches, N. HAADF-STEM Characterization and Simulation of Nanoparticle Distributions in an Inhomogeneous Matrix. *J. Microsc.* **2017**, *266* (1), 60−68.

(7) Pankhurst, Q. A.; Thanh, N. K. T.; Jones, S. K.; Dobson, J. Progress in Applications of Magnetic Nanoparticles in Biomedicine. *J. Phys. D: Appl. Phys.* **2009**, *42* (22), No. 224001.

(8) Pankhurst, Q. A.; Connolly, J.; Jones, S. K.; Dobson, J. Applications of Magnetic Nanoparticles in Biomedicine. *J. Phys. D: Appl. Phys.* **2003**, *36* (13), R167−R181.

(9) Ortega, D.; Pankhurst, Q. A. Magnetic Hyperthermia. In *Nanoscience*; O'Brien, P., Ed.; RSC Publishing, 2012; Vol. *1*, pp 60−88.

(10) Vall d'Hebron Institute of Oncology Vall d'Hebron Enrolls the First Patient in a Clinical Trial Designed to Treat Locally Advanced Pancreatic Cancer with Nanoparticles, 2022 https://www.vallhebron.com/en/news/news/vall-dhebron-enrolls-first-patient-clinical-trial-designed-treat-locally-advanced-pancreatic-cancer-nanoparticles. (accessed May 2024).

(11) Spanish Agency of Medicines and Medical Devices—AEMPS Clinical Study: "A Feasibility Clinical Investigation of Intratumoral Injection of Magnetic Nanoparticles Associated to Hyperthermia Treatment in Locally Advanced Pancreatic Cancer", 2022 https://oncotrialstrack.vhio.net/clinical_trial/Nocanther. (accessed May 2024).

(12) Wells, J.; Kazakova, O.; Posth, O.; Steinhoff, U.; Petronis, S.; Bogart, L. K.; Southern, P.; Pankhurst, Q. A.; Johansson, C. Standardisation of Magnetic Nanoparticles in Liquid Suspension. *J. Phys. D: Appl. Phys.* **2017**, *50* (38), No. 383003.

(13) Kallumadil, M.; Tada, M.; Nakagawa, T.; Abe, M.; Southern, P.; Pankhurst, Q. A. Suitability of Commercial Colloids for Magnetic Hyperthermia. *J. Magn. Magn. Mater.* **2009**, *321* (10), 1509−1513.

(14) Jonasson, C.; Schaller, V.; Zeng, L.; Olsson, E.; Frandsen, C.; Castro, A.; Nilsson, L.; Bogart, L. K.; Southern, P.; Pankhurst, Q. A.; Morales, M. P.; Johansson, C. Modelling the Effect of Different Core Sizes and Magnetic Interactions Inside Magnetic Nanoparticles on Hyperthermia Performance. *J. Magn. Magn. Mater.* **2019**, *477*, 198−202.

(15) Blanco-Andujar, C.; Ortega, D.; Southern, P.; Pankhurst, Q. A.; Thanh, N. T. K. High Performance Multi-Core Iron Oxide Nano-particles for Magnetic Hyperthermia: Microwave Synthesis, and the Role of Core-to-Core Interactions. *Nanoscale* **2015**, *7* (5), 1768−1775.

(16) Martinez-Boubeta, C.; Simeonidis, K.; Makridis, A.; Angelakeris, M.; Iglesias, O.; Guardia, P.; Cabot, A.; Yedra, L.; Estrade, S.; Peiro, F.; Saghi, Z.; Midgley, P. A.; Conde-Leboran, I.; Serantes, D.; Baldomir, D. Learning from Nature to Improve the Heat Generation of Iron-Oxide Nanoparticles for Magnetic Hyperthermia Applications. *Sci. Rep.* **2013**, *3*, No. 1652.

(17) Henkel, O. Remanence behavior and interactions in hard magnetic particle collectives. *Phys. Status Solidi (B)* **1964**, *7* (3), 919−929.

(18) Batlle, X.; del Muro, M. G.; Labarta, A. Interaction effects and energy barrier distribution on the magnetic relaxation of nanocrystalline hexagonal ferrites. *Phys. Rev. B* **1997**, *55*, No. 6440.

(19) Kaur, M.; Dai, Q.; Bowden, M.; Engelhard, M. H.; Wu, Y.; Tang, J.; Qiang, Y. Watermelon-like iron nanoparticles: Cr doping effect on magnetism and magnetization interaction reversal. *Nanoscale* **2013**, *5* (17), 7872−7881.

(20) Pérez, S.; Chanzy, H. Electron crystallography of linear polysaccharides. *J. Electron Microsc. Tech.* **1989**, *11* (4), 280−285.

(21) Easo, S. L.; Mohanan, P. V. Dextran stabilized iron oxide nanoparticles: Synthesis, characterization and *in vitro* studies. *Carbohydr. Polym.* **2013**, *92* (1), 726−732.

(22) Wells, J.; Kazakova, O.; Posth, O.; Steinhoff, U.; Petronis, S.; Bogart, L. K.; Southern, P.; Pankhurst, Q. A.; Johansson, C. Standardisation of magnetic nanoparticles in liquid suspension. *J. Phys. D: Appl. Phys.* **2017**, *50* (38), No. 383003.

(23) Chanzy, H.; Guizard, C.; Sarko, A. Single-crystals of dextran: 1. Low-temperature polymorph. *Int. J. Biol. Macromol.* **1980**, *2* (3), 149−153.

(24) Guizard, C.; Chanzy, H.; Sarko, A. The molecular and crystal-structure of dextrans: A combined electron and X-ray diffraction study. 2. A low-temperature, hydrated polymorph. *J. Mol. Biol.* **1985**, *183* (3), 397−408.

(25) Guizard, C.; Chanzy, H.; Sarko, A. Molecular and crystal-structure of dextrans: A combined electron and X-ray diffraction study. 1. The anhydrous high-temperature polymorph. *Macromolecules* **1984**, *17* (1), 100−107.

(26) Dekking, F.; Kraaikamp, C.; Lopuhaä, H.; Meester, L. The Poisson Process. In *A Modern Introduction to Probability and Statistics, Understanding Why and How*; Springer, 2005; pp 167−179.

(27) Wohlfarth, E. P. Relations between different modes of acquisition of the remanent magnetization of ferromagnetic particles. *J. Appl. Phys.* **1958**, *29* (3), 595−596.

(28) Bogart, L. K.; Blanco-Andujar, C.; Pankhurst, Q. A. Environmental oxidative aging of iron oxide nanoparticles. *Appl. Phys. Lett.* **2018**, *113* (13), No. 133701.